Pergamon

Ann. occup. Hyg., Vol. 39, No. 5, pp. 573–589, 1995
Elsevier Science Ltd

0003-4878/95 $9.50 + 0.00

0003–4878(95)00029–1

THREE-DIMENSIONAL FINITE-ELEMENT SIMULATION OF A TURBULENT PUSH–PULL VENTILATION SYSTEM

Michael R. Flynn, Kwangseog Ahn and Cass T. Miller

Department of Environmental Sciences and Engineering, University of North Carolina at Chapel Hill, Chapel Hill, NC 27599–7400, U.S.A.

(*Received in final form* 6 *February* 1995)

Abstract—A finite-element formulation with penalty approach to enforce continuity is employed here to simulate the three-dimensional velocity field resulting from a simple push–pull ventilation configuration. An analytic expression for the length scale and a transport equation for turbulent kinetic energy are coupled with the momentum equations. A coaxial square hood and jet are arranged with cross-draught perpendicular to the common centreline. Numerical predictions of the velocity and turbulence kinetic energy fields are evaluated in the plane of symmetry with hot film anemometry, and smoke-wire flow visualizations. The agreement of the simulated jet trajectories with flow visualizations is reasonable, as are velocities. Predictions of turbulence kinetic energy are not as good, particularly near the hood face. Despite the limitations the numerical approach is useful in assessing the impact of cross-draughts on the push–pull arrangement.

INTRODUCTION

Push–pull ventilation systems rely upon a jet of air to transport hazardous airborne pollutants to an exhaust hood for removal from the indoor environment. These systems are employed to capture mists and gases released from open surface tanks used in electroplating operations (ACGIH, 1992), or contaminants emitted from other industrial processes (Hughes, 1990). The purpose for installing such systems is to minimize human exposure to airborne pollutants, hence the time-integrated breathing-zone concentration is the appropriate index of system performance. A major factor in estimating such concentrations is the air velocity field that results from the interaction of a turbulent jet, a local exhaust hood (i.e. a source of suction), and any perturbing cross-draughts. This configuration represents the essential fluid mechanics for many contaminant-control ventilation problems.

A finite-difference study of push–pull systems by Heinsohn *et al.* (1986) produced encouraging yet limited results due to the two-dimensional treatment, however the complex geometry of real systems makes simulation of their performance quite challenging. The large linear algebra problem that results makes it desirable to use efficient, relatively simple approximations.

This work is motivated by the desire to develop a computer code to serve as a design and analysis tool specifically for push–pull ventilation systems. However, the algorithm should have the potential for extension to general indoor air pollution problems, which are also incompressible, three-dimensional and turbulent. The objectives here are to predict the three-dimensional velocity field of a simple push–pull configuration, and to examine these predictions with experimental data. Although most flows of industrial importance are time dependent, this investigation is restricted to a steady situation.

Three separate problems are examined. First, simulation of a free square jet is selected as a test problem. The aims are to predict the velocity and turbulence kinetic energy fields, and to examine these predictions with published data. Second, the trajectory of a square jet in a uniform cross-draught is modelled and compared with published data. Finally, the code is extended to include a hood and jet with a cross-draught perpendicular to the common axis. Hot film anemometry, flow visualization and tracer gas studies are conducted to examine these simulations.

THEORY

The governing equations are:

(i) incompressible continuity (conservation of mass)

$$\nabla \cdot \mathbf{u} = 0; \tag{1}$$

(ii) Navier–Stokes (conservation of linear momentum)

$$\mathbf{u} \cdot \nabla \mathbf{u} + \nabla P - \nabla \cdot [\nu_e (\nabla \mathbf{u} + \nabla \mathbf{u}^T)] = 0, \tag{2}$$

where $\mathbf{u}$ is the velocity vector, P is the dynamic pressure and ν_e is the effective kinematic viscosity, i.e. the sum of the laminar kinematic viscosity (ν) and the turbulent kinematic viscosity (eddy viscosity, ν_t). All variables are rendered dimensionless by reference to the jet inlet velocity U_0, the inlet half-width S, and the density of air at standard conditions. The eddy viscosity is defined by the Kolmogorov–Prandtl approximation:

$$\nu_t = C_2 \Lambda k^{1/2}, \tag{3}$$

where k is the kinetic energy of turbulence, C_2 is a constant and Λ is a length scale, reported by Sykes *et al.* (1986) for a circular jet as:

$$\Lambda = 0.25 D_j + 0.025 (x^2 + y^2 + z^2)^{1/2}. \tag{4}$$

Here D_j is the jet diameter and the origin of the co-ordinate system is at the centre of the jet face. Empirical work by duPlessis *et al.* (1974) suggests that the flow of a circular jet and square jet are close enough so that substitution of $2S$ for D_j in Equation (4) should be a reasonable approximation when S is the half-width of an equivalent area square jet.

The governing equation for k is:

$$\mathbf{u} \cdot \nabla k = \nu_t [\nabla \mathbf{u} \cdot (\nabla \mathbf{u} + \nabla \mathbf{u}^T)] + \nabla \cdot (\nu_t \nabla k) - A_2 \frac{k^{3/2}}{\Lambda} + \nu \nabla^2 k \tag{5}$$

and this model assumes the turbulence kinetic energy Prandtl number is unity. Values proposed in Sykes *et al.* (1986) for C_2 and A_2 of 0.35 and 0.7, respectively, are used throughout. For the push–pull simulations values of 0.18 and 0.5, respectively, are also used without any significant differences being observed.

METHODS

Numerical

The following weighted residual formulation for the momentum equations, uses a form suitable for spatially varying viscosity. A similar procedure is applied to the

conservation equation for the kinetic energy of turbulence. A penalty formulation is employed to eliminate pressure from the governing equations. The resulting approximation is:

$$P = -\lambda(\nabla \cdot \mathbf{u}), \tag{6}$$

where $\mathbf{u}$ and P now represent perturbed values for velocity and pressure. The penalty parameter (λ) is set to 10^7, see for example Hughes *et al.* (1979).

The appriopriate weak form, Gunzburger (1989), for the situation where surface tractions vanish on those boundaries of the domain where velocity Dirichlet conditions are not specified is:

$$\int_\Omega \left[N_l \hat{u}_J \frac{\partial \hat{u}_i}{\partial x_J} - \lambda \frac{\partial N_l}{\partial x_i}\frac{\partial \hat{u}_J}{\partial x_J} + \hat{v}_e \left(\frac{\partial N_l}{\partial x_J}\frac{\partial \hat{u}_i}{\partial x_J} + \frac{\partial N_l}{\partial x_J}\frac{\partial \hat{u}_J}{\partial x_i} \right) \right] d\Omega = 0. \tag{7}$$

The i index refers to a given momentum equation and J indicates an implied summation from Equations (1)–(3). Thus the x-momentum equation is obtained by letting $i = 1$ and each term in Equation (7) with a J subscript will have three terms in its expansion. The l index identifies the node, and (n_n) is the total number of nodes in the system.

The weighting functions employed are the trilinear Lagrange polynomial basis functions, N. A trial solution is:

$$\hat{u} = \sum_{m=1}^{n_n} N_m(\mathbf{x}) u_m. \tag{8}$$

A similar derivation for the turbulence kinetic energy yields:

$$\int_\Omega \left\{ N_l \left[\hat{u}_J \frac{\partial \hat{k}}{\partial x_J} - \hat{v}_t \frac{\partial \hat{u}_i}{\partial x_J}\left(\frac{\partial \hat{u}_i}{\partial x_J} + \frac{\partial \hat{u}_J}{\partial x_i} \right) \right] \right\} + \left\{ \hat{v}_t \left[\frac{\partial N_l}{\partial x_J}\frac{\partial \hat{k}}{\partial x_J} - N_l \frac{A_2}{C_2 \Lambda^2} \hat{k} \right] + \nu \frac{\partial N_l}{\partial x_J}\frac{\partial \hat{k}}{\partial x_J} \right\} d\Omega = 0. \tag{9}$$

In both momentum and turbulence equations upwinding is employed by reduced quadrature of the advective terms as outlined in Hughes *et al.* (1979). Non-linearity is handled by successive substitution with an under-relaxation factor of 0.5 on all velocity components and 0.8 for the turbulence kinetic energy. Three-dimensional brick elements are employed with trilinear basis functions. In this study local and global co-ordinate axes are coincident. Therefore reduced quadrature for the penalty terms was simpler than a consistent formulation, and of comparable accuracy [Engelman *et al.* (1982)]. Wall functions are used to enforce the no-slip boundary condition.

A special technique is used to handle the potential core region of the jet. In a free jet this region extends approximately five jet diameters downstream and is a zone of relatively constant velocity. Our interest is primarily in situations where the ratio of jet exit velocity to cross-draught velocity is large. In this case the potential core of the jet exists much as it does in a free jet. Since this is a very small portion of the domain, the centreline velocity is fixed in the core at a value of unity, and a technique described by Pelletier (1984) for specifying the turbulence kinetic energy in the core is employed.

These equations and boundary conditions are incorporated into a FORTRAN

Table 1. Grid refinement studies

Level	NELX	NELY	NELZ	B.W.	NEQS	u	v	w	k
Free jet									
L1	8	8	12	1023	4212				
L2	11	11	15	1815	9216				
L3	14	14	17	2295	16 200				
L1–L2						0.32	0.33	0.03	0.04
L2–L3						0.32	0.33	0.008	0.003
Push–pull with cross-draught									
R1	19	8	12	1023	9360				
R2	22	9	14	1295	13 800				
R3	25	10	17	1687	20 592				
R1–R2						0.44	0.50	0.16	0.37
R2–R3						0.26	0.18	0.16	0.54

NELX, -Y, -Z = number of elements in each direction.
B.W. = bandwidth.
NEQS = number of equations.

code and run on a Cray Y-MP. A convergence criterion of 0.001 is used for both velocity and turbulent kinetic energy. The error criterion, α, is defined as the relative change in the solution vector from one iteration to the next for a given dependent variable, for example in the case of turbulence kinetic energy,

$$\alpha = \frac{\left[\sum_{j=1}^{n_n} (k_j^{i+1} - k_j^i)^2\right]^{1/2}}{\left[\sum_{j=1}^{n_n} (k_j^i)^2\right]^{1/2}}, \tag{10}$$

here i is the iteration number and j the global node number. The same type of error is calculated in the grid refinement studies reported in Table 1. In this case i denotes the level of grid refinement and j represents nodes common to all refinement levels.

Experimental

For the free square jet and the jet deflected by a cross-draught, code predictions are examined using data published by other investigators. For push–pull systems, data gathered in this study are used to examine the simulations. Three specific techniques are employed: (1) hot film anemometry to measure velocity vectors and turbulence kinetic energy; (2) flow visualization by smoke wire technique to estimate flow streamlines and the jet trajectory; and (3) tracer gas studies to measure the efficiency with which the hood captures the jet.

The air velocity is measured using an X-probe, hot film anemometer mounted in a rotating support so that the probe axis can be aligned with the velocity vector. A simultaneous sampling module is employed to permit the calculation of turbulence kinetic energy from the sampled data. All measurements are made in a plane of symmetry where mean velocities are essentially two-dimensional.

The experimental configuration is shown in Fig. 1. A 9 cm (3.54 in.) square inlet is cut into a 61 cm (24 in.) square flange to serve as the exhaust hood. In a similar fashion

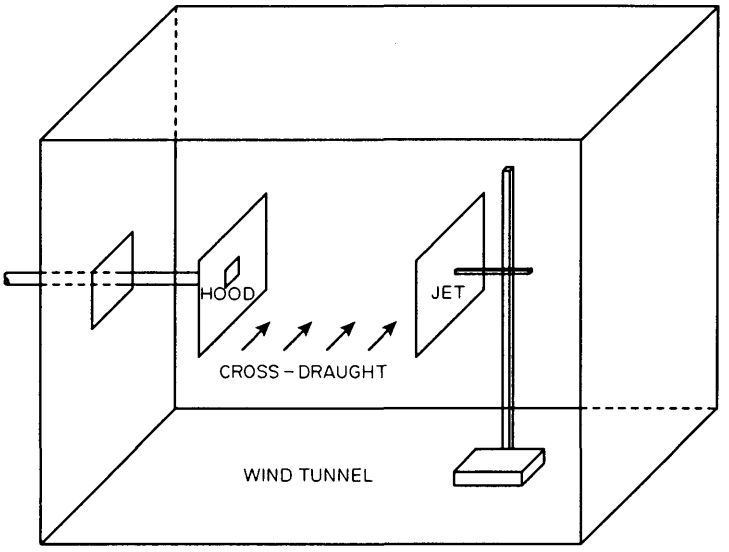

Fig. 1. Experimental set-up.

a 0.488 cm (0.192 in.) square jet is placed flush in the centre of another identical flange. The jet and hood are aligned along a common centreline and spaced 40.6 cm (16 in.) apart. The entire unit is placed within a 1.5 m (5 ft) square wind tunnel. Measurements of velocity are made at fixed points in the vicinity of the hood as shown in Fig. 2. The hood flow is 0.24 $m^3 s^{-1}$ (510 cfm) and in all cases the jet flow is 0.00082 $m^3 s^{-1}$ (1.75 cfm). Nominal cross-draughts of 0.51 m s^{-1} (100 fpm) and 1.27 m s^{-1} (50 fpm) are used. Hood flow is measured using a calibrated orifice plate, and the jet flow is monitored with a calibrated rotameter. Flow visualization is accomplished by coating a thin nichrome wire with paraffin oil and heating it electrically, a thin plane of smoke is then generated upstream of the push–pull system.

For the tracer gas studies dilute sulphur hexafluoride gas is metered into the jet and the concentration is measured in the duct downstream of the hood at a well mixed location. By forming the ratio of this concentration to the concentration when all of the jet is captured by the hood, that is the jet is placed inside the hood, a percentage capture efficiency is reported. This technique permits a quantitative validation of the jet trajectory. Measurement of concentration was made with a calibrated i.r. spectrophotometer. All tracer measurements were made with a round hood and jet with areas equal to those of the square hood and jet, in addition the round jet was unflanged. Although these conditions differ slightly from the simulations it was felt they were represented reasonably by the model.

RESULTS AND DISCUSSION

Figure 3(a) shows the computational domain for both the free square jet and Fig. 3(b) shows the domains for both the jet in a cross-draught and also the push–pull in a cross-draught. Points M, N, L and P are specified as the hood, only for the push–pull in the cross-draught case.

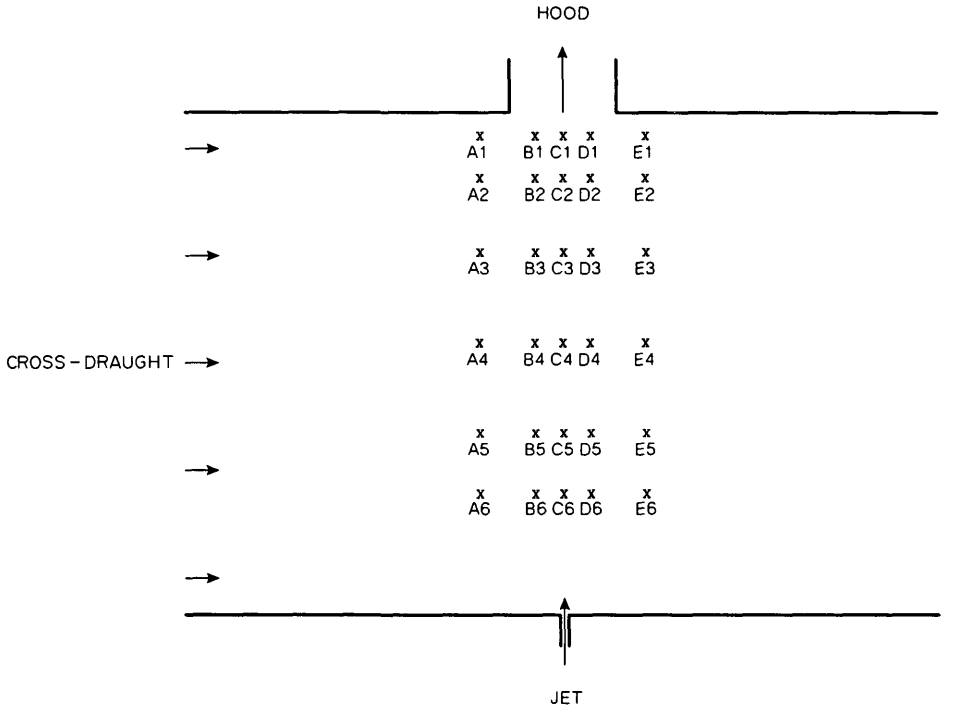

Fig. 2. Measurement locations for push–pull with cross-draught study.

The free square jet

Figure 3(a) shows the computational domain for the free jet. The origin of the Cartesian system is at the centre of the jet face (point A) and the z axis is the jet centreline (A–D). Only one quadrant of the flow field is modelled and the $x=0$ (ACED) and $y=0$ (AHJD) planes are planes of symmetry.

The remaining boundary conditions are: (1) the free surface planes at $x=X_1$ (HIKJ), and $y=Y_1$ (CIKE) are planes of zero tangential stress with the normal velocity a degree of freedom; (2) at the jet face (ABGF) $u=v=0$, $w=1$, and based on previous numerical work on jets by Demuren (1983), $k=0.001$; (3) for the remainder of the face (ACIH): $z=0$ and $u=v=w=k=0$; and (4) at the outflow boundary, $z=Z_1$ (DEKJ), surface tractions are assumed to vanish. The jet inlet velocity is 15.2362 m s^{-1} with a half-width (S) of 6.35 mm (0.025 in.); $X_1=Y_1=50S$, $Z_1=166.7S$.

Table 1 summarizes the grid refinement studies. The number of elements in each direction (NELX, -Y, -Z), the bandwidth (B.W.) and the number of equations (NEQS) is given for each level of refinement in the first section of the table. The error, α, for each degree of freedom is reported in the second section. The grids employ variable spacing to accommodate regions of anticipated steep gradients. The turbulence kinetic energy, and the z velocity behave well with respect to refinement, however x and y velocity components show some residual fluctuations.

Figure 4 shows predictions of jet centreline velocity plotted against data for a square jet presented by duPlessis *et al.* (1974) and Yevdjevitch (1966). The agreement is reasonable particularly in the far-field regions. Figure 5 shows predictions for the

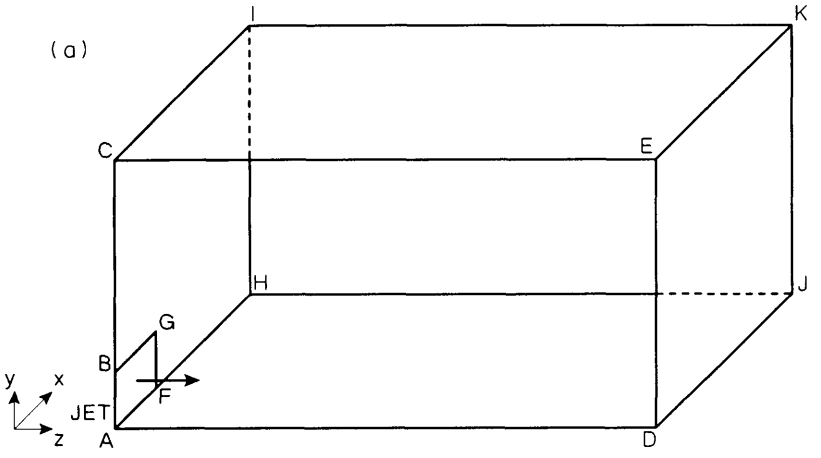

POINT	X	Y	Z
A	0	0	0
B	0	S	0
C	0	Y_1	0
D	0	0	Z_1
E	0	Y_1	Z_1
F	S	0	0
G	S	S	0
H	X_1	0	0
I	X_1	Y_1	0
J	X_1	0	Z_1
K	X_1	Y_1	Z_1

Fig. 3 (a).

growth of the jet half-width, and the experimental data reported by duPlessis *et al.* (1974) and Wygnanski and Fiedler (1969). The jet half-width at a given axial location is the distance perpendicular to the jet centreline at which the axial velocity has dropped to one half the value of the centreline velocity. Agreement in the far field region is good but in the near field the code tends to overpredict the half-width. A far-field value for the eddy viscosity is given by Schlichting (1979) as 0.032. At $Z/S=113$ and 130, mean values for the eddy viscosity taken over the jet half-width are 0.034 and 0.033, respectively, with coefficients of variation of 14 and 10%.

Jet and cross-draught

The square jet in a cross-draught requires a computational domain of one-half the actual region due to symmetry. Figure 3(b) illustrates this domain. Boundary conditions for the jet face (FGBO); the flange (i.e. the remainder of the face ACIH), and the core region are the same as for the free jet. The cross-draught velocity, U_c, was specified as the normal velocity on both the inflow face ACED and the outflow boundary HIKJ, tangential components were set to 0. The turbulence kinetic energy was set to $0.004(U_c)^2$ on ACED. For faces CIKE and DEKJ the cross-draught was specified as the tangential velocity and normal stresses were set to zero.

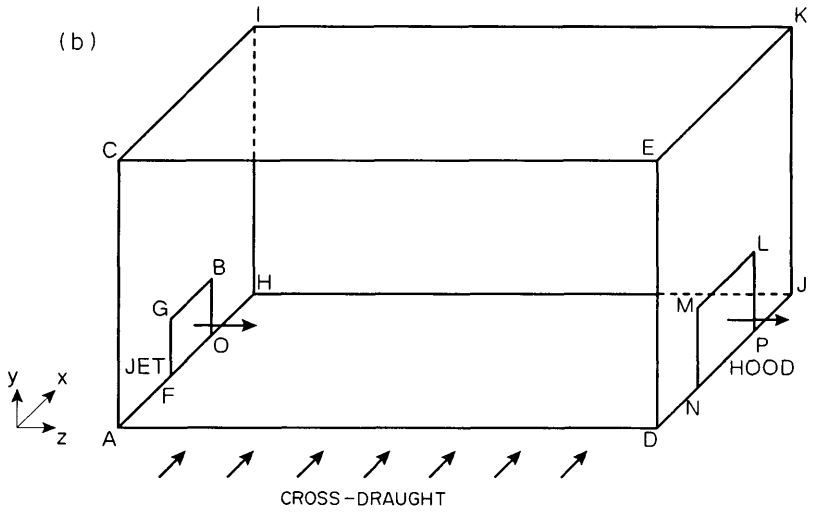

POINT	X	Y	Z
A	X_1	0	0
B	1.0	1.0	0
C	X_1	Y_1	0
D	X_1	0	Z_1
E	X_1	Y_1	Z_1
F	-1.0	0	0
G	-1.0	1.0	0
H	X_3	0	0
I	X_3	Y_1	0
J	X_3	0	Z_1
K	X_3	Y_1	Z_1
L	X_2	X_2	Z_1
M	$-X_2$	X_2	Z_1
N	$-X_2$	0	Z_1
O	1.0	0	0
P	X_2	0	Z_1

Fig. 3 (b).

Fig. 3. (a) Computational domain for free square jet problem. (b) Computational domain for jet in cross-draught and also push–pull with cross-draught.

Figure 6 shows the predicted velocity field in the plane of the cross-draught and Fig. 7 gives an estimate of the jet trajectory from this data compared to the experimental trajectory reported by Kamotani and Greber (1972). The jet trajectory is defined as the locus of maximum velocities in the plane of the cross-draughts. The agreement is reasonable but the predictions tend to have more momentum than the data suggest.

Push–pull with cross-draught

Finally a cross-draught perpendicular to the common hood-jet axis is added and Fig. 3(b) shows the computational domain. A uniform cross-draught velocity equal to

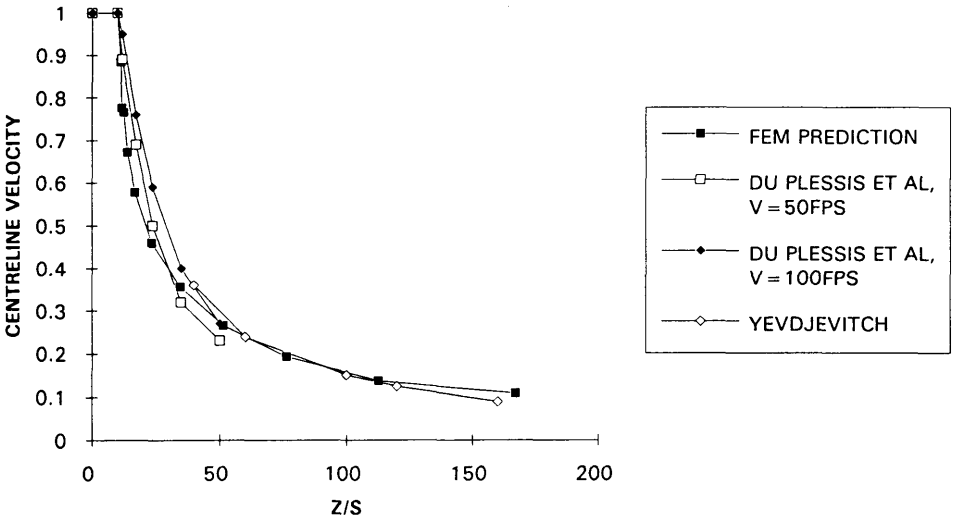

Fig. 4. Centreline velocity devay comparisons for free square jet.

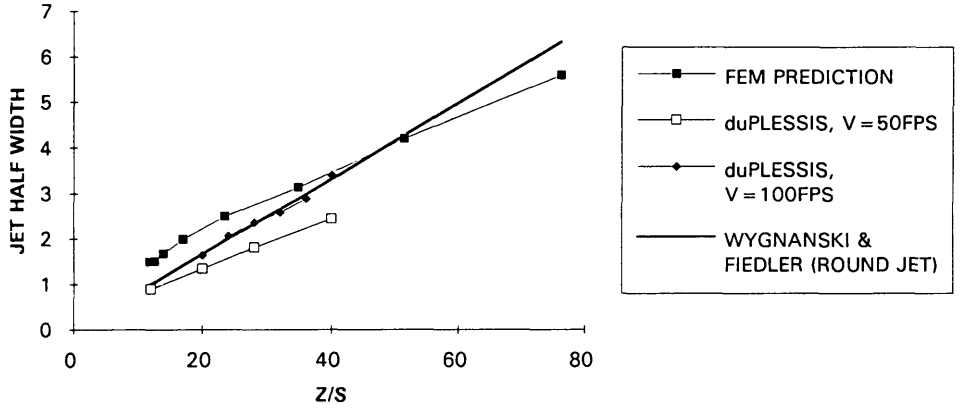

Fig. 5. Growth of half-width comparisons for free square jet.

the sum of the hood and wind tunnel flows divided by the tunnel cross-sectional area is specified as the upstream boundary condition (ACED). An outlet velocity is specified on (HIJK) by mass balance.

For these simulations $S = 2.39$ mm and $X_2 = Y_2 = \text{EXHLF} = 18.78S$, $X_1 = -6(\text{EXHLF})$, $X_3 = 8(\text{EXHLF})$; $Y_1 = -X_1$. The average jet inlet velocity (U_0) is 34.7 m s^{-1}; the average hood face velocity is 28.1 m s^{-1}, and outlet velocities on (HIJK) are either 0.51 m s^{-1} (100 fpm) or 1.27 m s^{-1} (250 fpm). The hood-to-jet separation is $Z_1 = 40.67$ cm.

Figures 8(a) and (b) present vector plots in the plane of symmetry (i.e. the plane of cross-draught, AHJD) for both cross-draughts. An estimate of the jet trajectory is included in the figures (dotted lines) based on the flow visualization photographs

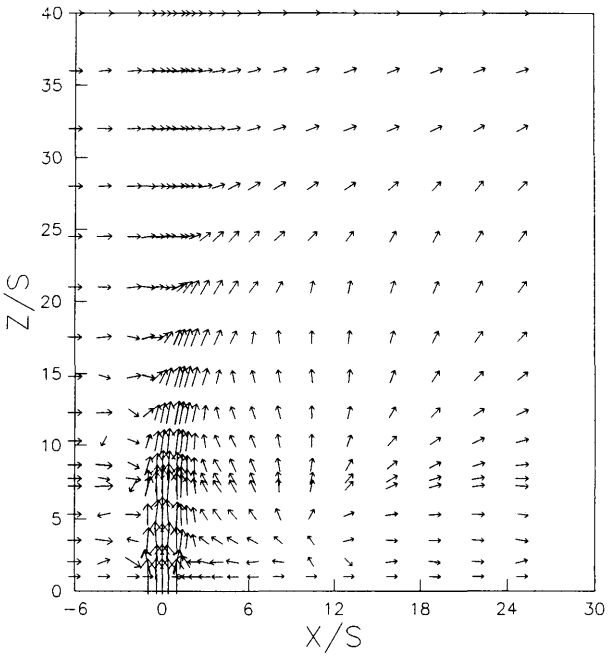

Fig. 6. Predicted velocity field for square jet in cross-draught, ratio of jet exit velocity to cross-draught velocity is 8.

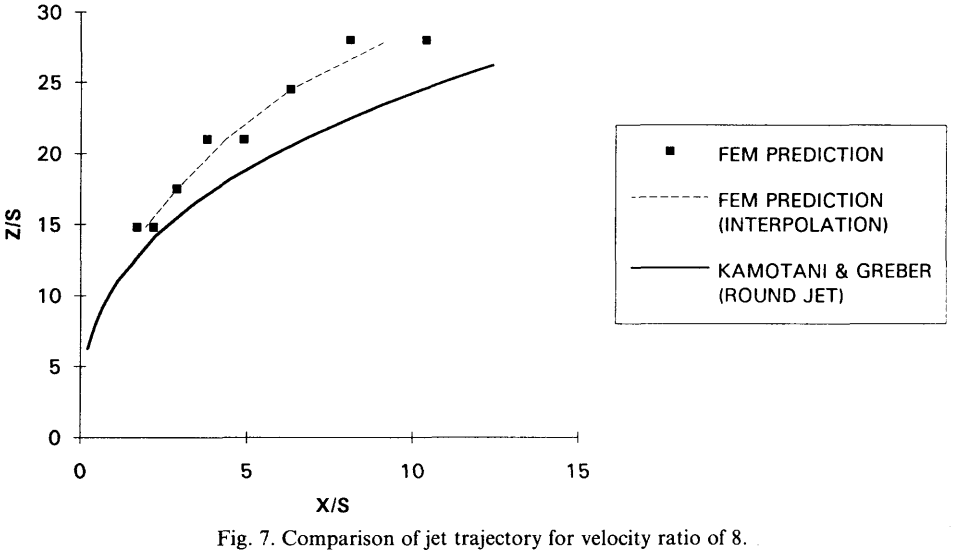

Fig. 7. Comparison of jet trajectory for velocity ratio of 8.

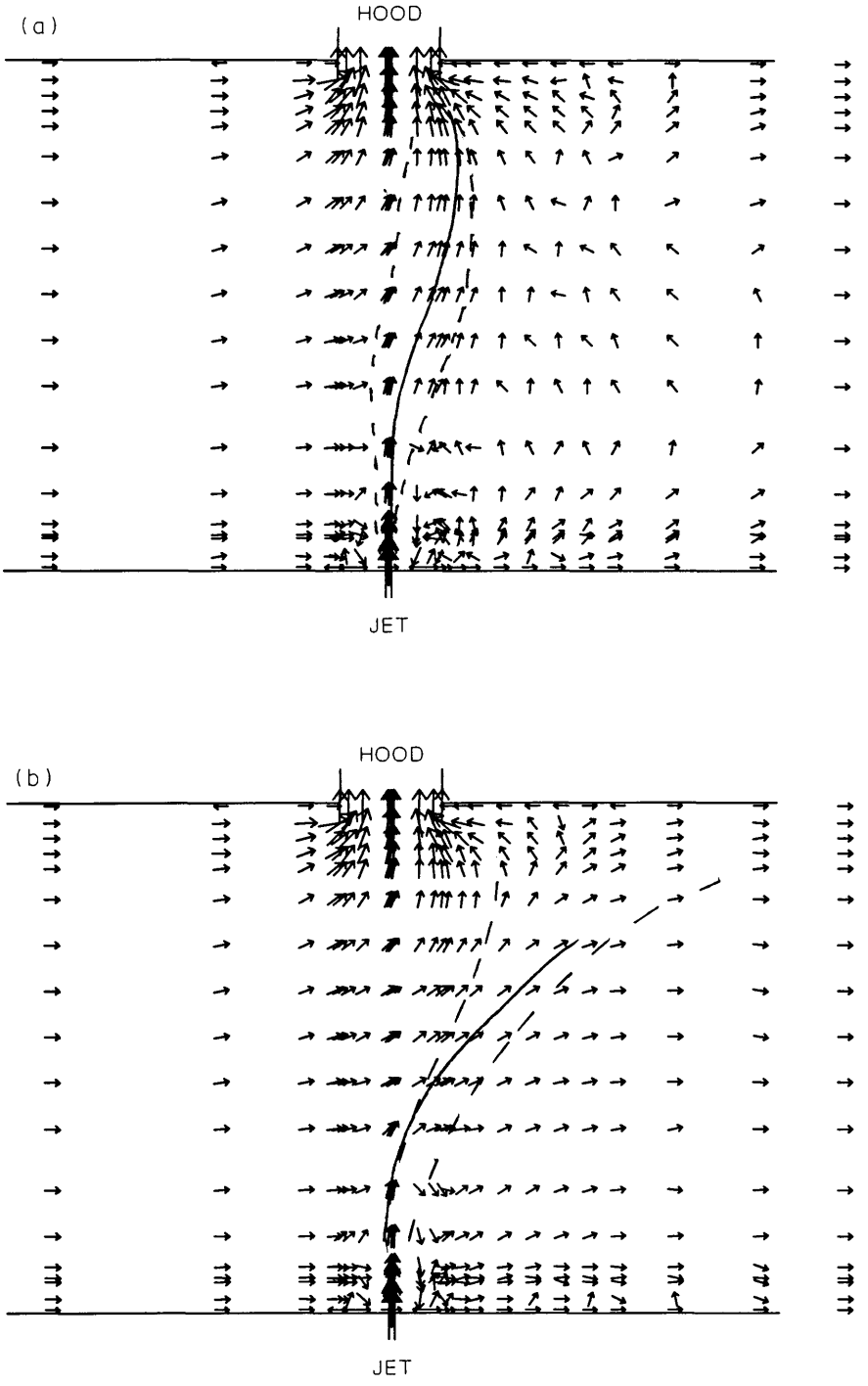

Fig. 8. (a) Predicted velocity field in the plane of cross-draught for push–pull system with 100 fpm cross-draught. (b) Predicted velocity field in the plane of cross-draught for push–pull system with 250 fpm cross-draught.

shown in Figs 9(a) and (b). Computer estimated jet trajectories (solid lines) are in reasonable agreement with the visualized trajectories. The lower cross-draught does not seem to deflect the jet substantially and one would expect most of the jet to be captured by the hood. Capture efficiency was measured at 82% for these conditions. The higher cross-draught deflects the jet to the point where less than half would be captured; efficiency here is measured at 60%.

In Figs 6 and 8(a) and (b) there are regions of the flow where the velocity vectors are clearly inaccurate, they are misaligned or pointing in directions opposite to what would be anticipated. These regions are generally near walls or boundaries, or in areas of steep velocity gradients. The memory limitations imposed on this algorithm by a fully coupled formulation prevents detailed grid refinement in these areas. In addition the turbulence model selected may be inadequate to correctly model these areas. Despite these inaccuracies, the local errors do not seem to unduly effect the global predictions of the jet trajectory.

Figures 10 and 11 present plots of all the measured vs experimental velocities and angles at the points shown in Fig. 2. Here the angle is measured in the x–z plane counterclockwise from the $-x$ axis. The maximum deviations between measured velocity vectors and model predictions occur at points D5, D6, E5 and E6. Examination of vector plots in Figs 8(a) and (b) show that these regions are poorly resolved by the grid, and measurement shows them to be locations of high turbulence intensity. Thus there is uncertainty in both model and data. These outliers were extracted from the data set and a linear regression analysis performed on the natural logarithms of the measured value vs the prediction. Table 2 presents the results of these regressions giving the slope and intercept along with the 95% confidence intervals, and coefficients of determination (R^2).

The null hypothesis that the slope is 1 and the intercept is 0, that is equivalence between model and experiment, cannot be rejected for the angle comparisons at the higher cross-draught nor the velocity comparisons at the lower cross-draught. In addition the velocity comparisons at the higher cross-draught meet the slope criterion and just miss the intercept. Angle measurements at the lower cross-draught clearly do not meet the criterion.

Figure 12 presents a plot of the turbulence kinetic energy data. Here the scatter is quite dramatic and in general the model fails to predict the quantity well. The greatest errors appear to occur near the hood face as well as at the locations identified above. This may reflect inadequacies in the turbulence model as well as insufficient grid resolution. Table 1 shows the results of the grid refinement studies. The α values for each of the velocity components and the turbulence kinetic energy are presented for two subsequent mesh refinements (L1–L2 and L2–L3). All variables except the turbulence kinetic energy appear to be converging with grid refinement as indicated by the decreasing values of α, although the errors are still rather high, and in some cases do not change appreciably from one refinement to the next.

CONCLUSIONS

This work suggests reasonable three-dimensional velocity simulations can be obtained with an upwind finite-element code employing a penalty function. The momentum and turbulence kinetic energy equations are solved here in coupled form,

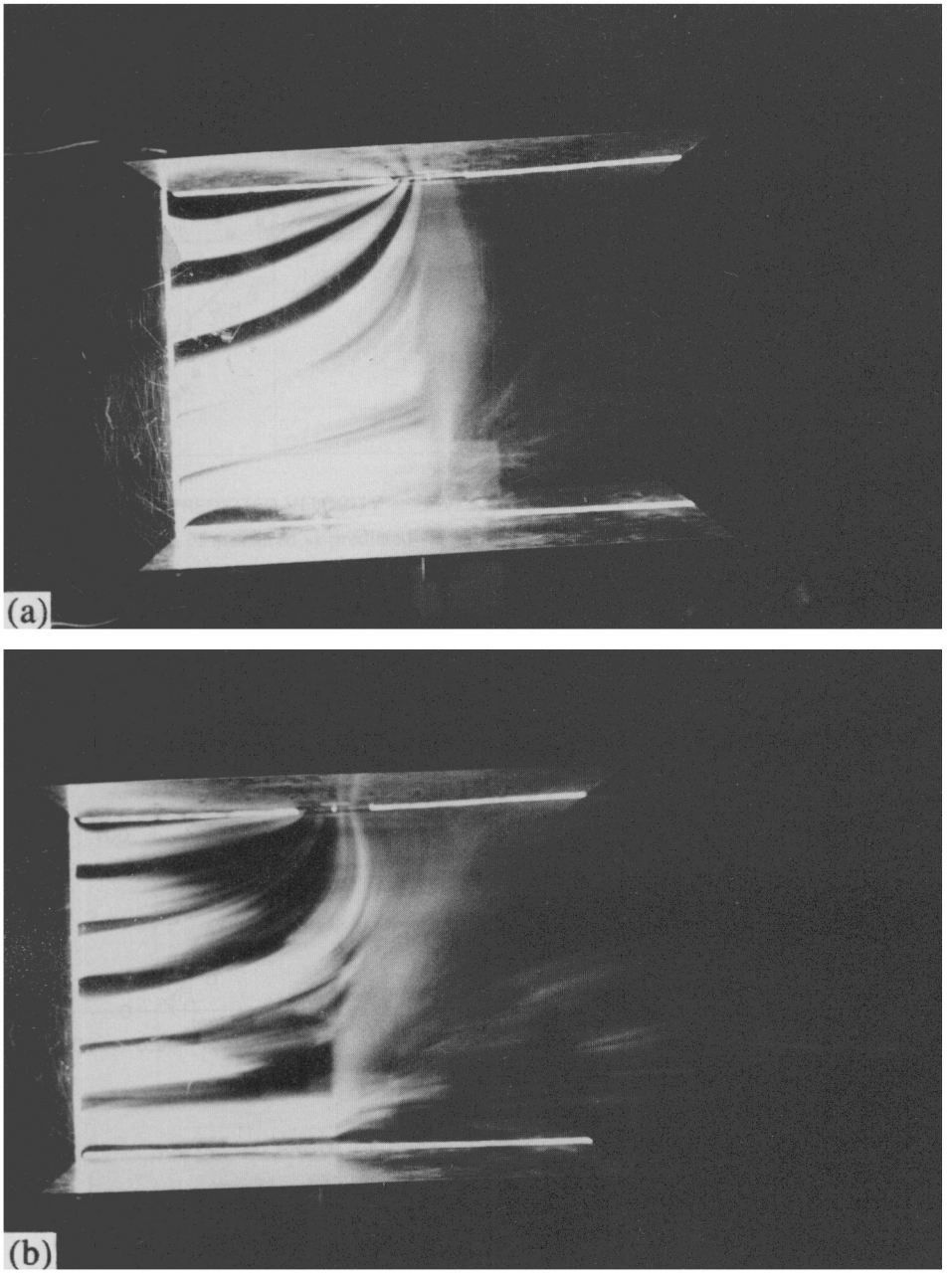

Fig. 9. (a) Smoke wire visualization in the plane of cross-draught for push–pull system with 100 fpm cross-draught. (b) Smoke wire visualization in the plane of cross-draught for push–pull system with 250 fpm cross-draught.

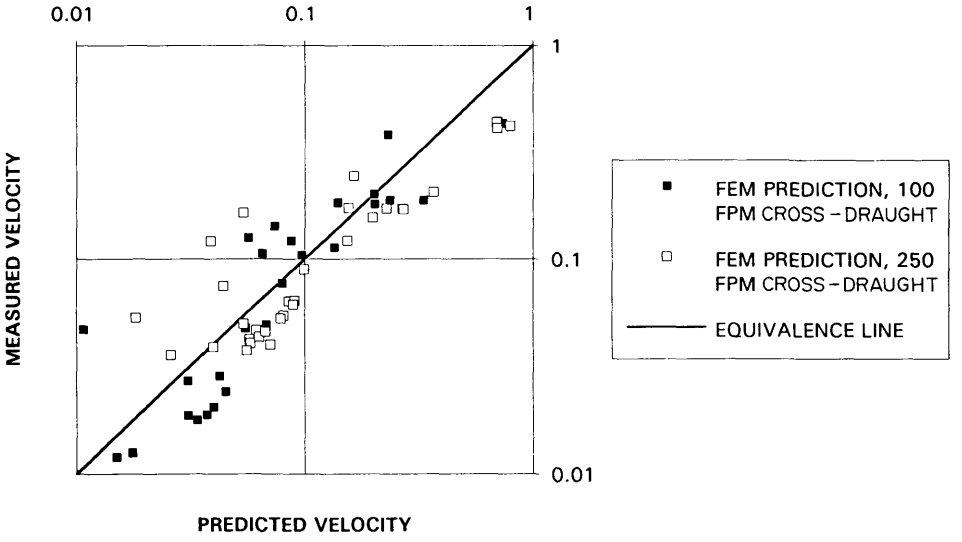

Fig. 10. Comparison of measured vs predicted velocities for push–pull in the plane of cross-draught.

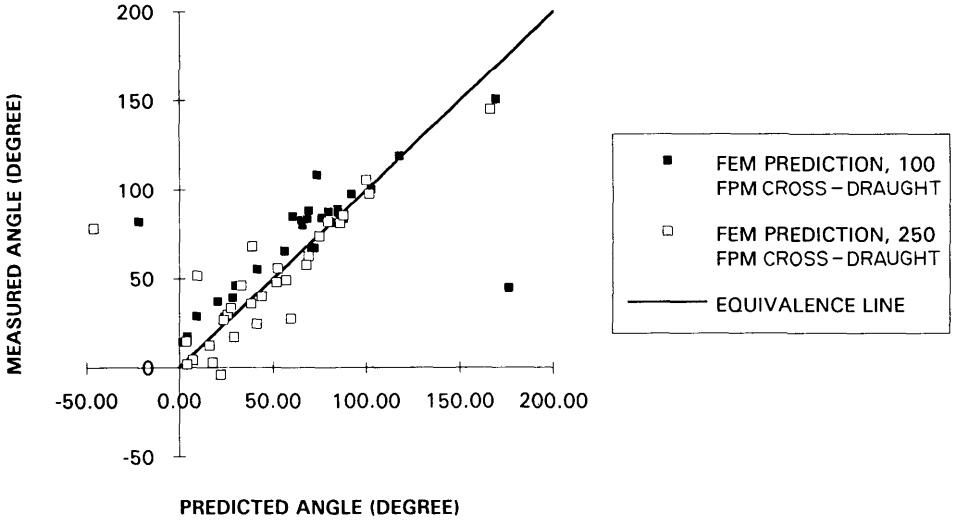

Fig. 11. Comparison of measured vs predicted angles for push–pull in the plane of cross-draught.

and produce a large coefficient matrix for solution. The direct solver employed here for three-dimensional calculations is limiting. Recent work by Reddy *et al.* (1992) suggests that iterative solvers are now possible with penalty formulations, and this should improve the competitiveness of the method with alternate approaches to modelling turbulent flows.

Despite limitations in the size of the problem that this algorithm can address, the agreement of the jet trajectory with the simulations is good. Agreement of predicted

Table 2. Regression analysis

Model: $Y = AX + B$,
where Y = natural log of measurement
X = natural log of prediction
A = slope
B = intercept

Variable	A	95% CI	B	95% CI	R^2
100 fpm cross-draughts					
Angle	0.55	[0.5, 0.6]	2.03	[1.8, 2.2]	0.95
Velocity	0.99	[0.8, 1.2]	−0.23	[−0.6, 0.2]	0.86
250 fpm cross-draught					
Angle	1.04	[0.8, 1.3]	−0.35	[−1.3, 0.6]	0.77
Velocity	0.89	[0.7, 1.0]	−0.5	[−0.8, −0.2]	0.89

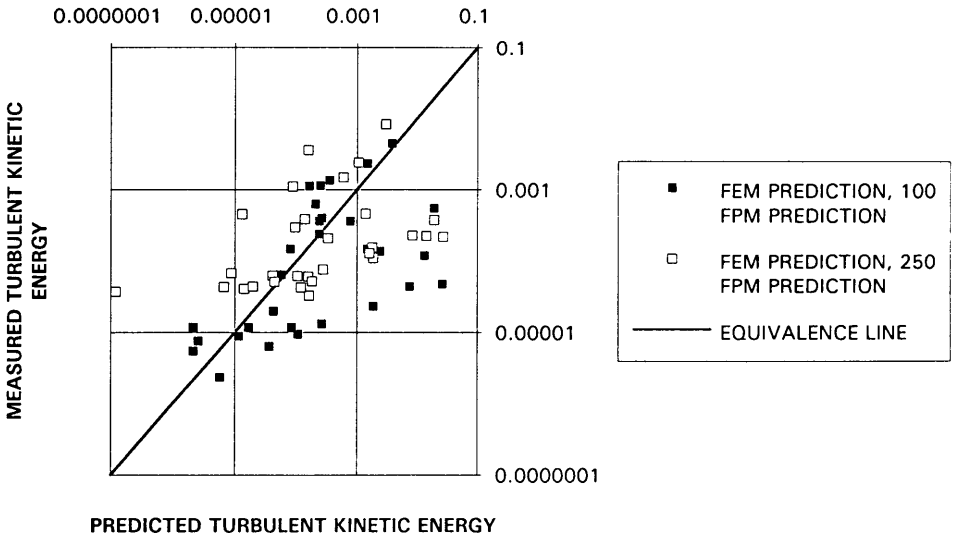

Fig. 12. Comparison of measured vs predicted turbulence kinetic energies for push–pull in the plane of cross-draught.

velocity magnitude and direction are reasonable, and the variation in turbulence kinetic energy is large. Further work is underway to improve the capacity of the code in order to evaluate the limitations of the turbulence model.

Acknowledgements—This work was supported by NIOSH grant 1-RO1 OH02710-01(2) entitled "Computer simulation of push–pull systems", and grants from the North Carolina Supercomputer Center.

REFERENCES

ACGIH (1992) *Industrial Ventilation a Manual of Recommended Practice* (21st Edn). American Conference of Governmental Industrial Hygienists, Lansing, Michigan.

Demuren, A. O. (1983) Numerical calculation of steady three dimensional turbulent jets in crossflow. *Comput. Meth. appl. Mech. Engng* **37,** 309–328.

duPlessis, M. P., Wang, R. L. and Kahawita, R. (1974) Investigation of the near-region of a square jet. *Trans. ASME J. Fluids Engng* Sept., 246–251.

Engelman, M. S., Sani, R. L., Gresho, P. M. and Bercovier, M. (1982) Consistent vs reduced integration penalty methods for incompressible media using several old and new elements. *Int. J. Numer. Meth. Fluids* **2,** 25–42.

Gunzburger, M. D. (1989) *Finite Element Methods for Viscous Incompressible Flows, A Guide to Theory, Practice and Algorithms*. Academic Press, New York.

Heinsohn, R. J., Yu, S. T., Merkle, C. L., Settles, G. S. and Huitema, B. C. (1986) Viscous turbulent flow in push–pull ventilation systems. In *Ventilation '85. Proc. 1st Int. Symp. on Ventilation for Contaminant Control*. Elsevier, Amsterdam.

Hughes, R. T. (1990) An overview of push–pull ventilation characteristics. *Appl. occup. Environ. Hyg.* **5,** 156–161.

Hughes, T. J. R., Wing, K. L. and Brooks, A. (1979) Finite element analysis of incompressible viscous flows by the penalty formulation. *J. Comput. Phys.* **30,** 1–60.

Kamotani, Y. and Greber, I. (1972) Experiments on a turbulent jet in a crossflow. *AIAA J.* **10,** 1425–1429.

Launder, B. E. and Spalding, D. B. (1974) The numerical computation of turbulent flows. *Comput. Meth. appl. Mech. Engng* **3,** 269–289.

McGuirk, J. J. and Rodi, W. (1979) The calculation of three-dimensional turbulent free jets. In *Turbulent Shear Flows* (Edited by Durst, F., Launder, B. E. *et al.*). Springer, New York.

Pelletier, D. (1984) Finite element solution of the Navier Stokes equations for three-dimensional turbulent free shear flows. Ph.D. Thesis, Virginia Polytechnic Institute and State University.

Reddy, M. P., Reddy, J. N. and Akay, H. U. (1992) Penalty finite element analysis of incompressible flows using element by element solution algorithms. *Compu. Meth. appl. Mech. Engng* **100,** 169–205.

Schlichting, H. (1979) *Boundary Layer Theory*. McGraw-Hill, New York.

Sykes, R. I., Lewellyn, W. S. and Parker, S. F. (1986) On the vorticity dynamics of a turbulent jet in a crossflow. *J. Fluid. Mech.* **168,** 393–413.

Wygnanski, I. and Fiedler, H. (1969) Some measurements in the self preserving jet. *J. Fluid Mech.* **38,** 577–612.

Yevdjevitch, V. J. (1966) Diffusion of slot jets with finite orifice length-to-width ratios. Hydraulics Papers. Colorado State University, Fort Collins, Colorado.